Inorganic Chemistry
Article
Cite This: Inorg. Chem. 2019, 58, 3861−3874
pubs.acs.org/IC

C−O and C−N Functionalization of Cationic, NCN-Type Pincer Complexes of Trivalent Nickel: Mechanism, Selectivity, and Kinetic Isotope Effect

Jean-Philippe Cloutier,[†] Lionel Rechignat,[‡] Yves Canac,[‡] Daniel H. Ess,[*,§] and Davit Zargarian[*,†]

[†]Département de chimie, Université de Montréal, Montréal, Québec H3C 3J7, Canada
[‡]LCC−CNRS, Université de Toulouse, CNRS, Toulouse, France
[§]Department of Chemistry and Biochemistry, Brigham Young University, Provo, Utah 84604, United States

Supporting Information

ABSTRACT: This report presents the synthesis of new mono- and dicationic NCN-Ni^{III} complexes and describes their reactivities with protic substrates. (NCN is the pincer-type ligand κ^N, κ^C, κ^N-2,6-$(CH_2NMe_2)_2$-C_6H_3.) Treating van Koten's trivalent complex (NCN)-$Ni^{III}Br_2$ with $AgSbF_6$ in acetonitrile gives the dicationic complex $[(NCN)Ni^{III}(MeCN)_3]^{2+}$, whereas the latter complex undergoes a ligand-exchange reaction with $(NCN)Ni^{III}Br_2$ to furnish the related monocationic complex $[(NCN)Ni^{III}(Br)(MeCN)]^+$. These trivalent complexes have been characterized by X-ray diffraction analysis and EPR spectroscopy. Treating these trivalent complexes with methanol and methylamine led, respectively, to C-OCH_3 or C-$NH(CH_3)$ functionalization of the Ni-aryl moiety in these complexes, C-heteroatom bond formation taking place at the *ipso*-C. These reactions also generate the cationic divalent complex $[(NCN)Ni^{II}(NCMe)]^+$, which was prepared independently and characterized fully. The unanticipated formation of the latter divalent species suggested a comproportionation side reaction between the cationic trivalent precursors and a monovalent species generated at the C−O and C−N bond formation steps; this scenario was supported by direct reaction of the trivalent complexes with the monovalent compound $(PPh_3)_3Ni^ICl$. Kinetic measurements and density functional theory analysis have been used to investigate the mechanism of these C−O and C−N functionalization reactions and to rationalize the observed inverse kinetic isotope effect in the reaction of $[(NCN)Ni^{III}(Br)(MeCN)]^+$ with CH_3OH/CD_3OD.

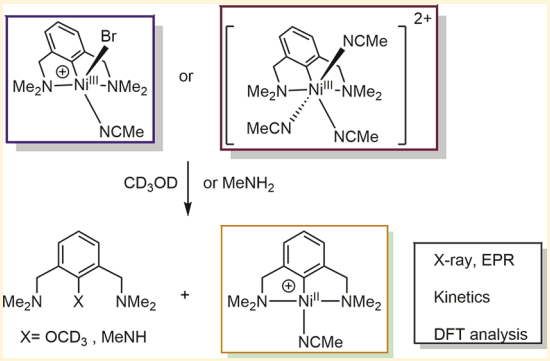

INTRODUCTION

Examples of Ni-promoted carbon−heteroatom coupling reactions are increasingly frequent in the literature.[1] Proposed mechanisms for C−O and C−N bond formation reactions often invoke the involvement of high-valent (Ni^{III} and Ni^{IV}) intermediates. The origins of this idea can be traced to seminal work by Hillhouse's group showing that Ni^{II} alkoxide and amide complexes undergo C−O and C−N reductive elimination upon oxidation.[2] More recent reports by Mirica have shown that Ni^{III} complexes can promote C−C and C−O functionalization of a Ni^{III}−Ar moiety,[3] whereas authentic Ni^{IV} complexes active in C−C, C−N, C−O, and C−S formation were isolated by the groups of Sanford[4a] and Nebra.[4b]

Our group's earlier work[5] showed that the divalent complex $(NCN^{pz})Ni^{II}Br$ bearing a pyrazine-flanked pincer ligand (NCN^{pz} = 1,3-bis(pyrazole)-C_6H_3) undergoes C−O/C−N functionalization at the aryl moiety of the pincer ligand when treated with alcohols or amines under aerobic conditions, or with H_2O_2 (Scheme 1). That aerobic conditions are essential for the observed C−X coupling reactivities of these compounds with alcohols or amines strongly indicated that these reactions go through high-valent intermediates, but no such species could be isolated.

Scheme 1. Previous Work on C-Heteroatom Coupling Promoted by a Ni^{II} Precursor

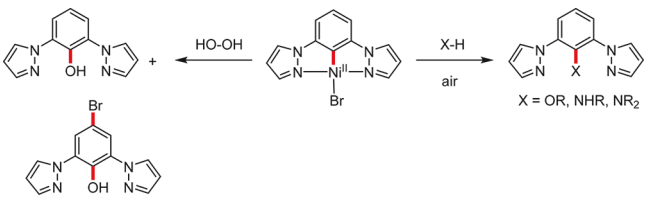

In a more recent follow-up study,[6] we reported that analogous C−O and C−N functionalizations take place at the *ipso*-C of the NCN ligand in $(NCN)Ni^{III}Br_2$ (NCN= κ^N, κ^C, κ^N-2,6-$(CH_2NMe_2)_2$-C_6H_3)[7] when this authenticated trivalent complex is treated with water, alcohols, and amines;

Received: December 14, 2018
Published: March 1, 2019

DOI: 10.1021/acs.inorgchem.8b03489
Inorg. Chem. 2019, 58, 3861−3874

this system also promoted the more difficult C-halogen functionalization reaction with HCl or HBr (Scheme 2).

Scheme 2. Previous Work on C-Heteroatom Coupling Promoted by a Ni^{III} Precursor

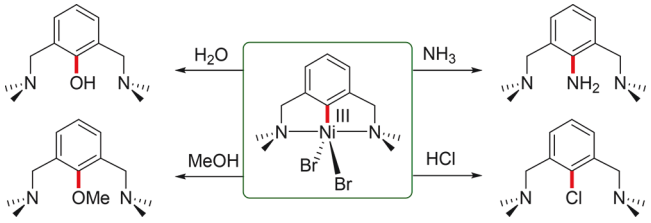

The two key steps in the proposed mechanism for the above functionalization reactions are the coordination of the protic substrate HX to the trivalent Ni center, followed by its deprotonation to generate the requisite Ni–X moiety. We reasoned that both of these steps should take place more readily with a more electrophilic, cationic Ni precursor. Indeed, involvement of cationic Ni^{III} intermediates in C–O coupling reactions has been postulated by MacMillan[1a] and demonstrated by Mirica.[3] We were thus inspired to prepare isolable and thermally stable cationic trivalent complexes and investigate their intrinsic reactivities toward protic substrates.

The present work reports the synthesis and characterization of new mono- and dicationic Ni^{III} complexes based on van Koten's NCN ligand and describes their reactions with methanol and methylamine to give C–O and C–N ligand functionalization under mild conditions. We also report a new cationic Ni^{II} capable of promoting aerobic C–O ligand functionalization, albeit slowly. Density functional theory (DFT) studies have revealed metal–ligand cooperativity in the deprotonation of MeOH and have shown that the C–O coupling step is the result of a reductive elimination process. As was the case in our previous report on the functionalization of the charge-neutral trivalent complex $(NCN)Ni^{III}Br_2$, the yields obtained from the reaction of cationic and dicationic complexes with MeOH under nitrogen never exceed 50%, implying a redox process taking place between the trivalent precursors and monovalent species generated at the reductive elimination step. DFT calculations confirm that this redox process is not only viable but crucial for rendering the C–O bond formation step irreversible. The reductive elimination is rate-limiting for both C–O and C–N coupling. The potential energy surface obtained for the reaction with methylamine shows that deprotonation is most likely assured by a second molecule of the substrate. Calculations also explain the observed inverse kinetic isotope effect by showing that coordination of CD_3OD is favored over that of CH_3OH.

RESULTS AND DISCUSSION

We began our studies by preparing the divalent cation $[(NCN)Ni(NCMe)]^+$, **1**, and testing its reactivity with methanol. This compound was prepared in 64% yield by using silver salts to abstract the Br^- in van Koten's divalent complex $(NCN)Ni^{II}Br$[8] and replacing it with acetonitrile (Scheme 3). The ^1H and ^{13}C NMR spectra of the resulting solid were consistent with the anticipated C_{2v} point group symmetry of the target cationic complex. (Some of the signals were also quite characteristic and facilitated monitoring the functionalization reactions; vide infra.) For instance, the ^1H NMR spectrum (C_6D_6) showed the anticipated triplet and doublet signals for the three aromatic protons (6.89 and 6.29 ppm; $^3J_{HH}$ = 7.5) and the two singlets for NCH_2 and NCH_3, at 2.76 and 2.20 ppm, respectively. The latter are shifted upfield by 0.33 ppm compared to the corresponding signals in the charge-neutral bromo precursor, whereas the singlet for Ni-$NCCH_3$ resonates close to the corresponding signal for free acetonitrile in C_6D_6 (0.62 vs 0.58 ppm). The most characteristic $^{13}C\{^1H\}$ signal was due to $Ni–C_{(Ar)}$ (~147 ppm). Single-crystal X-ray diffraction studies of **1** confirmed the anticipated square planar structure, which is also shown in Scheme 3; the most pertinent structural parameters are provided in the Supporting Information.

Scheme 3. Synthesis of $[(NCN)Ni^{II}(MeCN)]^+$ (1) and Its Reaction with Methanol

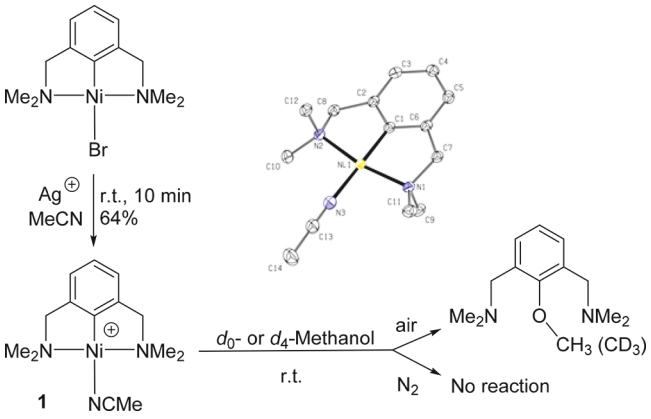

With **1** fully characterized, we proceeded to test its reaction with methanol. No reaction took place when **1** was stirred in CH_3OH or CD_3OD at room temperature *under* N_2, but conducting the same reactions *in air* led to slow formation of the demetalated coupling products, $NC(OCH_3)N$ or $NC(OCD_3)N$. For example, the latter was obtained in <5% after 2 h and ~11% after 24 h. The observation that aerobic functionalization of the Ni-aryl moiety is possible suggested that perhaps O_2 can induce oxidation of the Ni^{II} complex **1** to a dicationic trivalent Ni^{III} intermediate, a species that would be poised for methanol coordination and subsequent C–O coupling. Cyclic voltammetry measurements carried out on cationic complex **1** showed, not surprisingly, that it has a greater oxidation potential relative to its charge-neutral bromo precursor (724 vs 240 mV, ref Ag/AgCl; see the Supporting Information for CV trace), but we surmised that this complex should be prone to oxidation with strong oxidants. Thus, we set out to prepare trivalent analogues of **1** and study their reactivities toward protic substrates.

Synthesis of Mono- and Dicationic Trivalent Complexes. We targeted the cationic acetonitrile adducts $[(NCN)Ni^{III}(Br)(NCMe)_n]^+$ and $[(NCN)Ni^{III}(NCMe)_m]^{+2}$, because acetonitrile is known to stabilize divalent[9] and trivalent[3] Ni cations. To our surprise, several attempts at oxidizing **1** with $CuBr_2$ or $NOBF_4$ did not give the target mono- and dicationic trivalent species. Thus, we modified our synthetic strategy as follows: instead of oxidizing the divalent cation **1**, we prepared the previously reported charge-neutral, trivalent complex **2**[7] and ionized it subsequently by bromide abstraction in acetonitrile, as shown in Scheme 4.

Thus, treating **2** with two equivalents of Ag^+ allowed the isolation of the formally 19-electron octahedral dication

DOI: 10.1021/acs.inorgchem.8b03489
Inorg. Chem. 2019, 58, 3861–3874

Scheme 4. Syntheses of $[(NCN)Ni^{III}(MeCN)_3]^{2+}$ $2[SbF_6]^-$ (3) and $[(NCN))Ni^{III}(Br)(MeCN)]^+[SbF_6]^-$ (4)

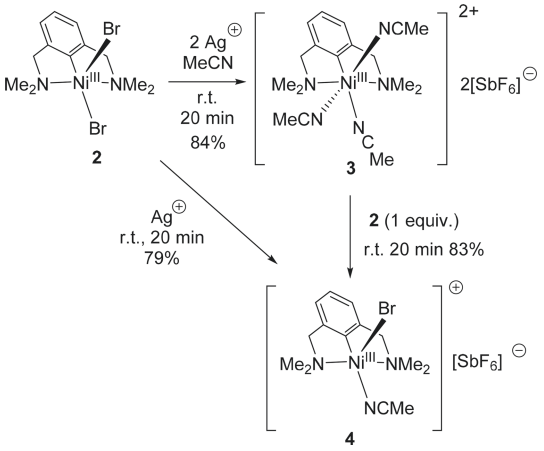

$[(NCN)Ni(NCMe)_3]^{2+}$, **3**, as an air-stable red powder in 84% yield (Scheme 4). It then occurred to us that this dication might undergo a ligand exchange reaction with its charge-neutral precursor **2** to generate a monocationic trivalent complex. Indeed, treatment of **3** with one equivalent of **2** furnished the monocation **4** as a deep purple solid in 83% yield (Scheme 4). The pentacoordinate, formally 17-electron complex **4** can also be obtained directly from the reaction of **2** with one equivalent of Ag^+ in 79% yield. Complexes **3** and **4** were fully characterized, including by single-crystal X-ray diffraction analysis (Figures 1 and 2) and EPR spectroscopy

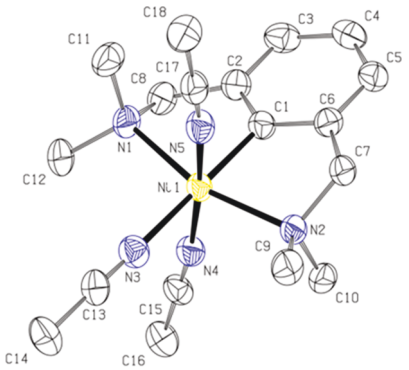

Figure 1. X-ray structure of **3**. Thermal ellipsoids are shown at the 50% level. The SbF_6 counteranions and all H atoms are omitted for clarity. Selected bond distances (Å) and angles (deg): Ni1–N1 = 2.122(4); Ni1–N2 = 2.099(4); Ni1–N3= 2.003(5); Ni1–N4 = 2.082(5); Ni1–N5= 2.086(5); Ni1–C1= 1.905(5); N1–Ni1–N2 = 161.34(17); C1–Ni1–N3 = 179.2(2); Ni1–N3–C13 = 177.5(5); Ni1–N4–C15 = 170.6(5); Ni1–N5–C17 = 169.4(5).

(vide infra). To our knowledge, these are the first examples of cationic Ni^{III} complexes featuring monoanionic, meridional ECE-type pincer ligands. Figures 1 and 2 show the X-ray structures of **3** and **4**, respectively, along with selected distances and angles.

Complex **3** adopts a distorted octahedral geometry in the solid state, whereas **4** displays a square pyramidal geometry with the Ni atom positioned ca. 0.42 Å out of the basal plane defined by C1, N1, N2, and N3 atoms. The main structural distortions in **3** and **4** are related to the very long axial Ni–N and Ni–Br distances[10] as well as the smaller-than-ideal trans

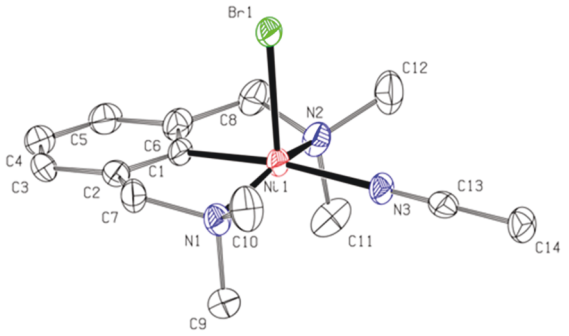

Figure 2. X-ray structure of **4**. Thermal ellipsoids are shown at the 50% level. The SbF_6 counteranion and all H atoms are omitted for clarity. Selected bond distances (Å) and angles (deg): Ni1–N1 = 2.013(4); Ni1–N2 = 2.011(4); Ni1–C1 = 1.873(4); Ni1–N3 = 1.978(4); Ni1–Br1 = 2.4014(8); N1–Ni1–N2 = 156.06(17); C1–Ni1–N3 = 171.56(16); C1–Ni1–Br1 = 90.31(12).

angles N_{NMe2}–Ni–N_{NMe2} that define the bite angle for the NCN ligand (161° in **3** and 156° in **4**). Comparison of the structural parameters in **3** and **4** to structurally related Ni^{III} species reported in the literature shows that the average Ni–NMe_2 distances are comparable to the corresponding distances of the octahedral $(NCN)Ni^{III}(py)(NCS)_2$ (2.110 vs 2.132 Å)[11] and the penta-coordinate dibromide **2**, $(NCN)NiBr_2$, (2.012 vs 2.039 Å).[12] The Ni–NCMe distance trans from the aryl moiety in **3** is also comparable to the corresponding distance found in the dicationic octahedral Ni^{III} species $[(^{t\text{-Bu}}N_3C)Ni(NCMe)_2]^{2+}$ reported recently by Mirica's group.[13] The Ni–C_{Ar} distance in the latter complex is also close to the corresponding distance in **4** (1.9018(1) vs 1.873(4) Å).

Complexes **3** and **4** were also analyzed by X-band EPR spectroscopy (Figures 3 and 4; Table 1). The EPR X-band spectrum of the dicationic Ni complex **3** shows a temperature-independent, broad signal lacking hyperfine structure (Figure 3, left). The simulated spectrum allowed us to determine three distinct g values, which confirmed the expected rhombicity for paramagnetic Ni^{III} complexes (Table 1 and Figure 3, right).[7] The cationic Ni complex **4** is also characterized by an isotropic broad signal at 293 K (Figure 4, top). In contrast to the relatively unchanged low-temperature spectrum observed for **3**, complex **4** displayed a dramatic change at 120 K with the appearance of an anisotropic signal featuring different hyperfine couplings. The high multiplicity of the frozen EPR spectrum of **4** cannot a priori be rationalized by the presence of a single paramagnetic Ni^{III} species. The most likely explanation is that the EPR signal is due to the coexistence of two stereoisomers, **4** and **5**, wherein the Br atom occupies, respectively, either the axial or the equatorial position of the plane defined by the C1, N1, N2, and N3 atoms. More precisely, the EPR spectrum of **4** exhibits high rhombicity with three distinct g values for each isomer (**4**: g_x = 2.269; g_y = 2.145; g_z = 2.027; **5**: g_x = 2.307; g_y = 2.090; g_z = 2.077). Hyperfine couplings to the Br atom (I = 3/2) are evidenced along the g_z direction in **4** (A_{Br} = 151.5 G), and along the g_x (A_{Br} = 27.6 G) and g_y (A_{Br} = 60.1 G) directions in **5** (Figure 4, bottom). On the basis of the best fit between experimental and simulated spectra, we propose that the two stereoisomers **4** and **5** exist in an approximately 3:1 ratio, with the major isomer **4** corresponding to the structure determined by X-ray diffraction analysis (see Figure 2).

DOI: 10.1021/acs.inorgchem.8b03489
Inorg. Chem. 2019, 58, 3861–3874

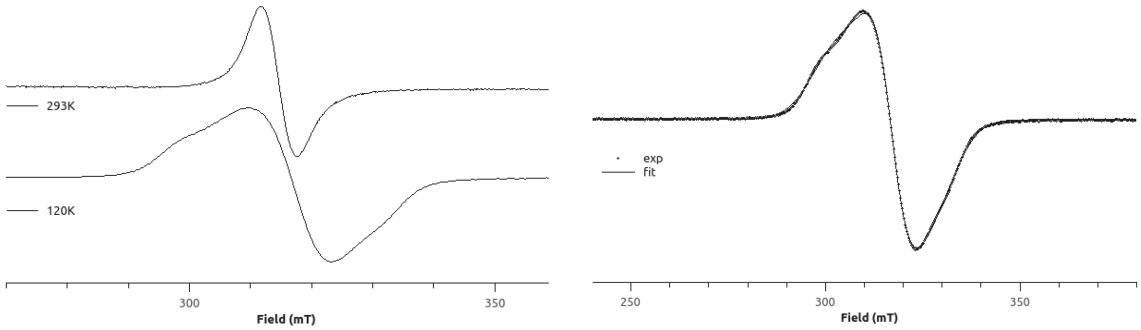

Figure 3. Experimental (MeCN, 293 and 120 K, left) and simulated (120 K, right) X-band EPR spectra of **3**.

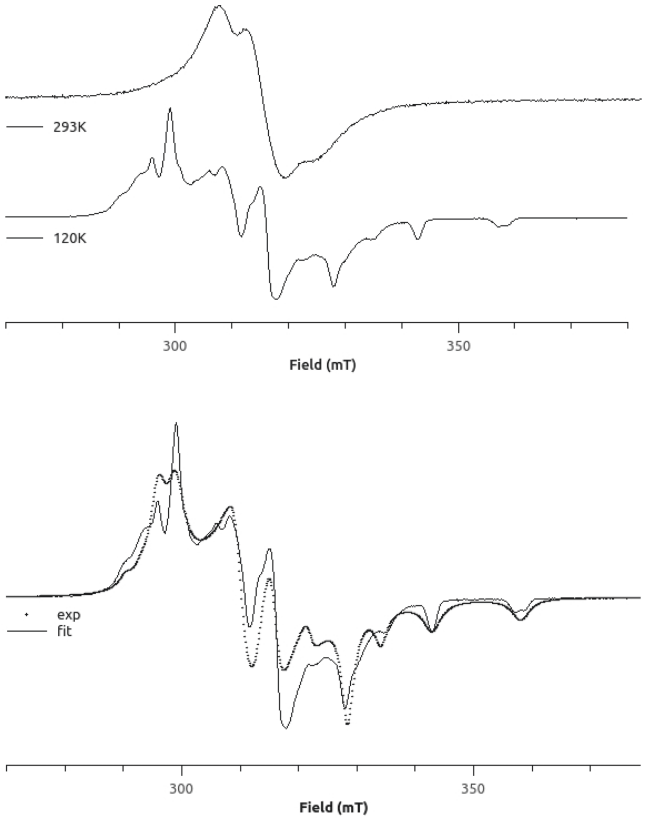

Figure 4. Experimental (MeCN/toluene, 293 K, and CH_2Cl_2/toluene, 120 K, top) and simulated (120 K, bottom) X-band EPR spectra of **4**.

Table 1. Data for the Experimental and Simulated EPR Spectra of 3 and 4

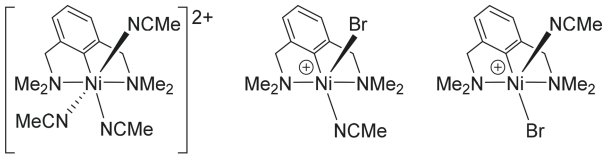

3 **4** **5**

complex	g_x	g_y	g_z	A_x[a]	A_y[a]	A_z[a]
3	2.247	2.144	2.073			
4	2.269	2.145	2.027			151.5
5	2.307	2.090	2.077	27.6	60.1	

[a]In Gauss.

The EPR spectra of both **3** and **4** revealed g values that are higher than the free electron g value 2.0023; this indicates the absence of significant ^{14}N coupling, thus supporting the localization of the unpaired spin density in an orbital bearing substantial metal character. This assessment was supported by DFT calculations (using UM06L/6-31G**), showing Mulliken spin density build-up on the nickel center with a value of 0.97 e/Å^3 for **3** (Figure 5). In the case of complex **4**, the Mulliken spin density values were 0.85 e/Å^3 on Ni and 0.20 e/Å^3 on Br. For complex **4**, the isomer shown in Figure 5 is only ∼4 kcal/mol lower in free energy than the alternative isomer **5** with acetonitrile and bromide positions switched; this finding is consistent with the presence of two species identified in the EPR spectrum.

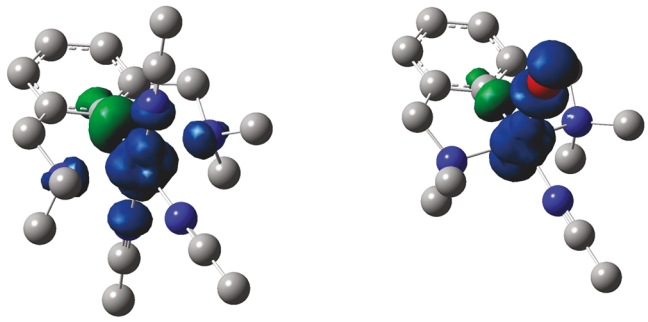

Figure 5. Alpha spin density plots for complexes **3** (left) and **4** (right). Plots generated with an isovalue of 0.004 e/Å^3.

Reactivity of the Cationic Trivalent Species 3 and 4. As shown in Scheme 5, complexes **3** and **4** reacted readily (r.t.) with methanol and methyl amine to give C−O and C−N aryl-functionalization products. It is worth recalling here that the analogous functionalization of the divalent complex **1** requires aerobic conditions, whereas functionalization of the trivalent complexes **3** and **4** proceeds *under a nitrogen atmosphere*. The reactions with CD_3OD were monitored by ^1H NMR spectroscopy to establish functionalization rates relative to those observed with the cationic divalent species **1**. Given the NMR-silent nature of **3** and **4**, the reaction progress was based on monitoring the aromatic signals of the emerging functionalized product, i.e., the triplet at ∼7.3 ppm for *p*-H and/or the doublet at ∼7.5 ppm for *m*-H. While the products of the C-$NH(CH_3)$ coupling reactions could be isolated directly, isolation of the C-OCH_3 coupling products required extraction of the final reaction mixture with aqueous base to neutralize the in situ generated ammonium moiety. The results are discussed below.

DOI: 10.1021/acs.inorgchem.8b03489
Inorg. Chem. 2019, 58, 3861−3874

Scheme 5. Reactions of 3 and 4 in Neat CD_3OD or CH_3NH_2 (33% Solution in EtOH)

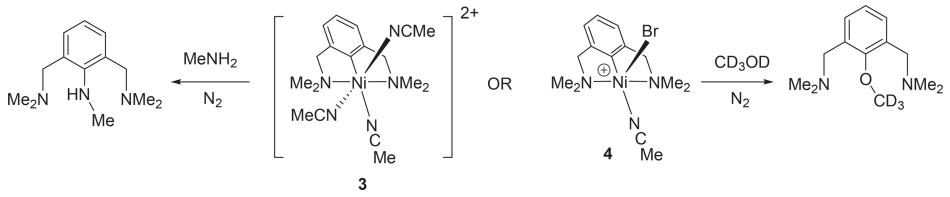

The C-OCD_3 functionalization of **3** and **4** gave different yields as a function of time and the presence of oxygen. For instance, under anaerobic conditions, we obtained 47% (**3**) and 7% (**4**) functionalization after 10 min; extending the reaction time to 2 h increased the yield for the reaction with **4** (42%), but the yield remained unchanged for the reaction with **3**. Conducting these C−O functionalization reactions under aerobic conditions gave very similar initial yields: 48% with **3** and 42% with **4** over 2 h. Interestingly, however, the reaction yields increased significantly with extended reaction times, going from 42% to 67% over 24 h with **4**, and from 48% to 73% over 96 h with **3**. The significance of obtaining higher than 50% yields for these aerobic reactions is discussed below.

A crucial observation was made for the reaction of CD_3OD with both mono- and dicationic complexes: in addition to the functionalized product $NC(OCD_3)N$, we detected the formation of the monocationic divalent species $[(NCN)\text{-}Ni^{II}(NCMe)]^+$, **1**; moreover, these two products formed in a 1:1 ratio. As shown in Scheme 6, we propose that this 1:1 ratio

Scheme 6. Reactivities of 3 and 4 in Support of Proposed Functionalization Mechanism

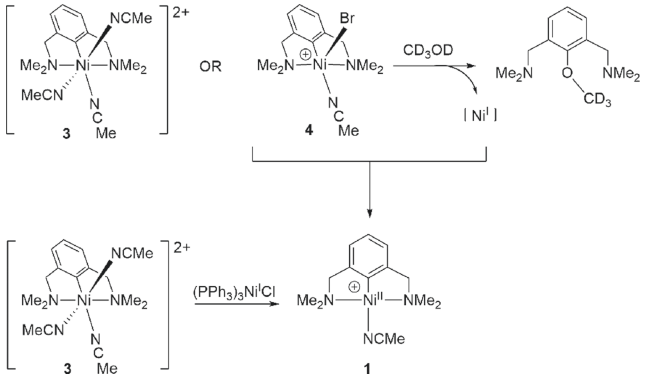

results from a comproportionation reaction between **3** or **4** and a Ni^I species that must be generated in situ as a side product of the reductive elimination step that furnishes the C−O coupling product.

To test the above hypothesis involving a comproportionation reaction, we prepared the known monovalent complex $(PPh_3)_3Ni^ICl$[13] and treated it with one equivalent of **3** in CD_3CN; as expected, this reaction generated the divalent cation **1** after 1 h. The signals for the latter were broad at first but became progressively well-defined after 15 h (see Figure S25). This finding, combined with the observation of a 1:1 ratio for the functionalized product $NC(OCD_3)N$ and **1**, supports the postulated comproportionation reaction between the Ni^{III} precursor and the in situ generated Ni^I. Moreover, we can conclude that this redox process is faster than the functionalization reaction itself, because a rate-limiting comproportionation would increase the yield of the functionalization product NC(OMe)N, which turns out not to be the case. Another observation consistent with the proposed comproportionation side reaction is the increase in yield observed with the extended reaction time under air: we believe that the in situ generated divalent cationic Ni **1** is responsible for giving higher yields of the C−O coupling product.

The kinetics of the functionalization reactions with methanol were measured by ^1H NMR (see the Supporting Information) and UV−visible spectroscopy (Figure 6), both approaches

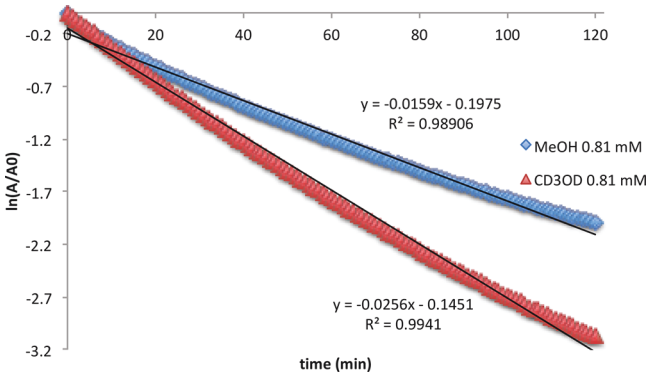

Figure 6. UV−visible spectroscopy time course profile for the reaction of a 0.81 mM solution of **4** with CH_3OH/CD_3OD.

revealing a first-order reaction with respect to Ni. Comparison of the rates for reactions conducted under otherwise identical conditions with CH_3OH or CD_3OD allowed us to measure the overall kinetic isotope effect of the C−O coupling reaction. Treating the trivalent monocationic species **4** with neat CH_3OH or CD_3OD and monitoring the decay of complex **4** by UV−vis spectroscopy gave a pseudo-first-order time profile with an overall k_H/k_D value of 0.62. This inverse kinetic isotope effect (KIE) is similar to the k_H/k_D value of 0.47 we measured for the reaction of complex **2** with CH_3OH/CD_3OD.[6]

The above results allow us to conclude that the C−O coupling is fastest with the dicationic, trivalent complex **3** (47% yield in 10 min), followed by its monocationic analogue **4** (42% yield in 2 h), and finally by the divalent monocation **1** (11% yield over 24 h), which suggests a strong correlation between the electrophilicity of the Ni center, on the one hand, and substrate uptake and reductive elimination rates on the other. Similarly, reactions of **3** and **4** with CH_3NH_2 (used as 33% solution in EtOH at r.t. and under N_2) led to rapid C−N bond formation (over 5 min) with yields of 15% with **3** and 21% with **4**. Running these reactions under aerobic conditions over 2 h gave the same yield for the C-$NH(CH_3)$ coupling product with **3** (16%), but a slightly higher yield was obtained with **4** (29% vs 21%). The following test confirmed that the poor yields observed in these C−N bond formation reactions are caused by rapid reduction of **3** and **4** by CH_3NH_2: indeed, reacting the dicationic complex **3** with the bulky amine *t*-

DOI: 10.1021/acs.inorgchem.8b03489
Inorg. Chem. 2019, 58, 3861−3874

$BuNH_2$ did not promote C−N functionalization, leading instead to the rapid formation of the divalent complex **1**.[14] It is noteworthy that no C−OEt coupling was observed for the reactions with CH_3NH_2 conducted in EtOH.

Density Functional Calculations: Ni^{III}/Ni^{IV} Oxidation Potential and Ni^{III} Orbital Characterization. The above-presented functionalizations of **3** and **4** with CH_3OH and CH_3NH_2 indicate that, contrary to what was observed with C-heteroatom functionalization promoted in air by the divalent precursors **1**, external oxidants are *not* essential for the C−O and C−N functionalization of these cationic Ni^{III} complexes. We have undertaken DFT calculations to improve our understanding of the mechanism of Ni-aryl bond functionalization in trivalent Ni complexes. Before analyzing the reactivities of **3** and **4** with CH_3OH and CH_3NH_2, we sought to verify that our computational approach would accurately model the Ni^{III} and higher oxidation states (Scheme 7). For all calculations in Gaussian 09,[15] geometries were optimized with UM06L/6-31G** with the continuum MeCN SMD solvent model.[16] Final electronic energies, with solvation, were evaluated using the Def2-TZVP basis set. For complex **3**, the M06L calculated Ni^{III}/Ni^{IV} oxidation potential is 1.21 V (calculated at 298 K relative to ferrocene), which is very close to the experimentally measured value of 1.18 V. Other functionals such as M06, B3LYP, and ωB97X-D gave values that were too large by >0.5 V (see the Supporting Information). For complex **4**, the calculated Ni^{III}/Ni^{IV} oxidation potential is 0.91, which is 0.15 V greater than the experimental value of 0.74 V. Again, other functionals showed significantly larger errors for estimating this oxidation potential.

Scheme 7. Ni^{III}/Ni^{IV} Redox Reactions at 298 K

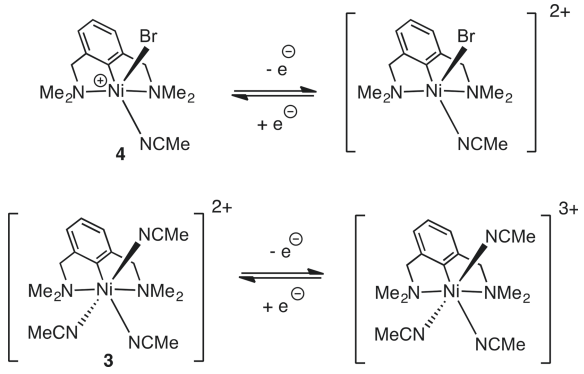

Figure 7 displays the α-spin and β-spin molecular orbitals of the formally 17 electron monocationic complex **4**. Analysis of the α-spin HOMO orbital shows that it is an antibonding combination of the Ni d_{z^2} and bromine p_z. This orbital description is consistent with the spin density plot in Figure 5. About 0.4 eV lower in energy than the α-spin HOMO, there are two degenerate α-spin HOMO−1 orbitals with d_{xz} and d_{yz} character and antibonding interactions with bromide p_x and p_y orbitals. The degenerate HOMO−2 orbital set is mainly ligand-centered, whereas the degenerate HOMO−3 set is Ni d-orbital based. Although the α-spin orbitals 95α, 94α, 93α, and 91α are significantly delocalized on the Br atom, they nevertheless provide four electrons to the Ni metal center. Similarly, there are three β-spin electrons with Ni d-character, two degenerate β-spin HOMOs and HOMO−3. Similar to the α-spin manifold, the pair of β-spin HOMOs is delocalized onto the Br atom.

Examining the formally 19-electron dicationic complex **3** in a similar manner yields the MO assignments shown in Figure 8. The α-LUMO is composed of the d_{z^2} orbital, and is σ antibonding with the phenyl ring. The α-spin HOMO consists

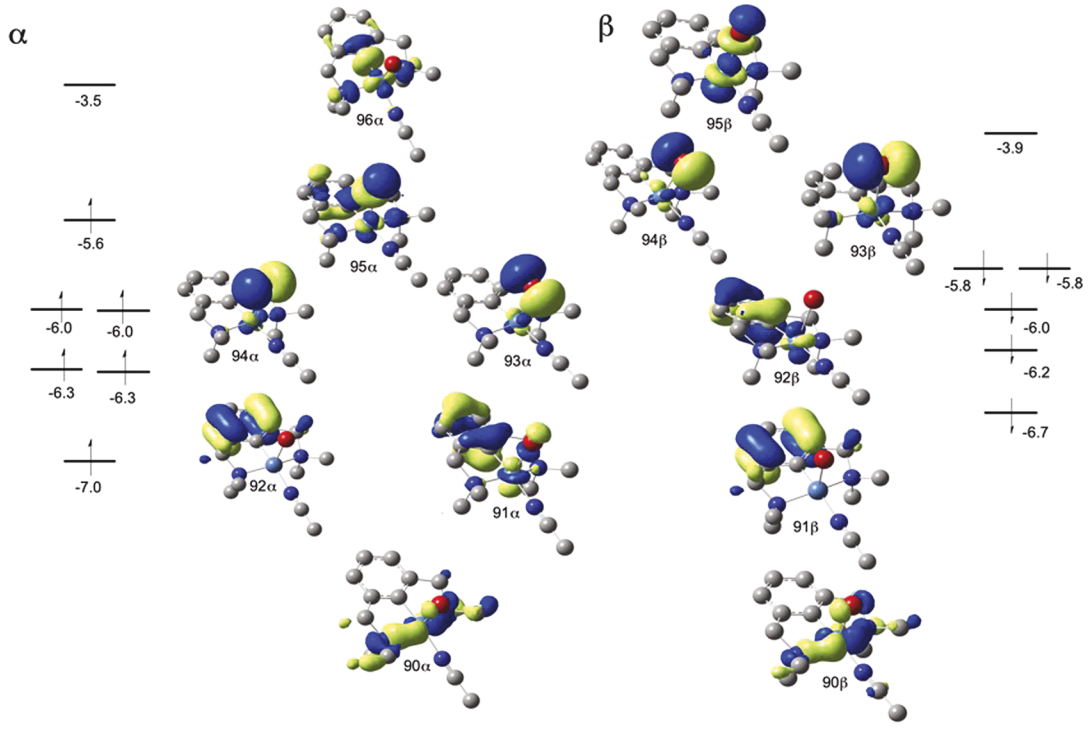

Figure 7. UM06-L α-spin and β-spin molecular orbitals for monocationic complex **4**. Orbital energies are reported in electronvolts.

DOI: 10.1021/acs.inorgchem.8b03489
Inorg. Chem. 2019, 58, 3861−3874

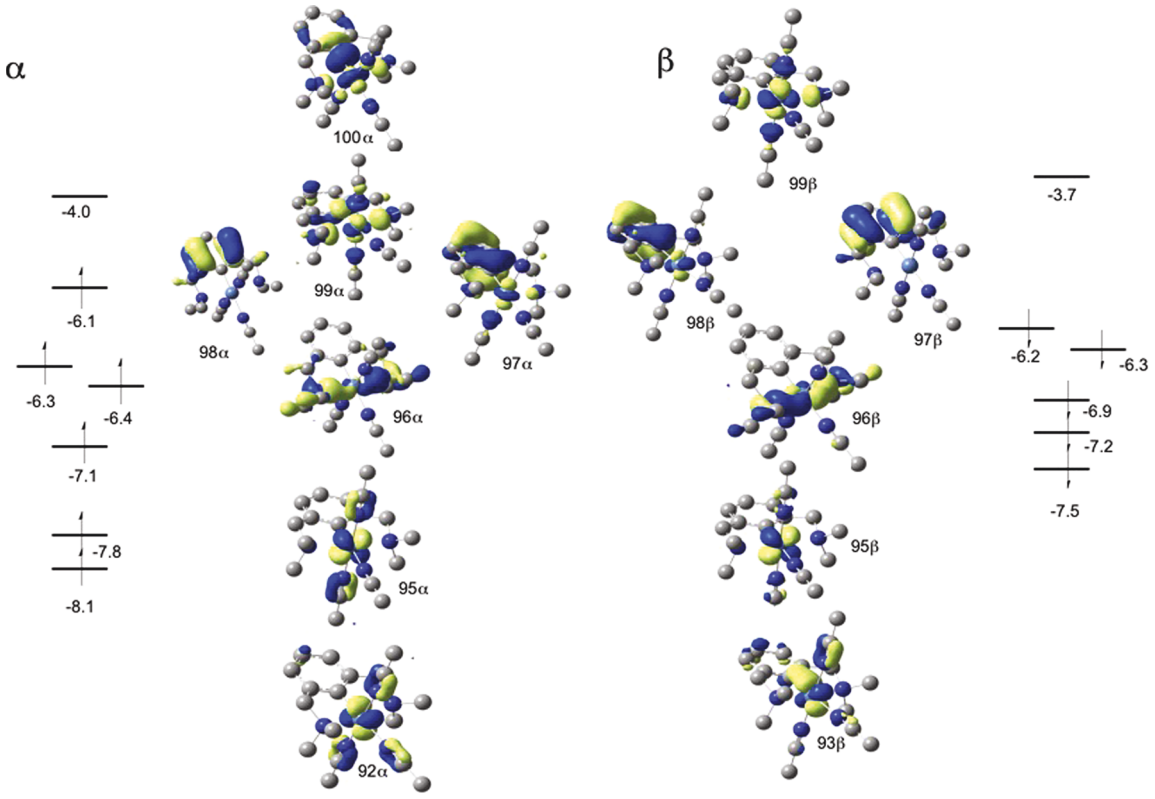

Figure 8. UM06-L α-spin and β-spin molecular orbitals for dicationic complex **3**. Orbital energies are reported in electronvolts.

Scheme 8. Simplified Mechanistic Proposal for C−O Coupling for Reaction between 4 and CH_3OH

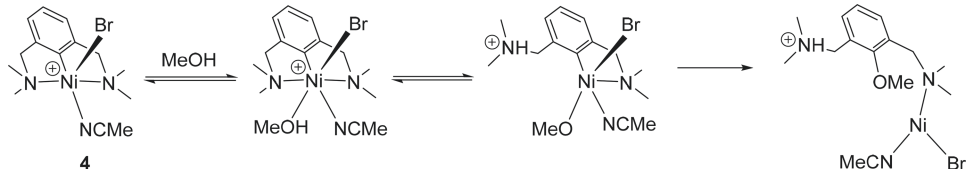

4

Scheme 9. Gibbs Free Energy (and Enthalpy) for CH_3OH Coordination and Substitution with Complex 4 (kcal/mol)

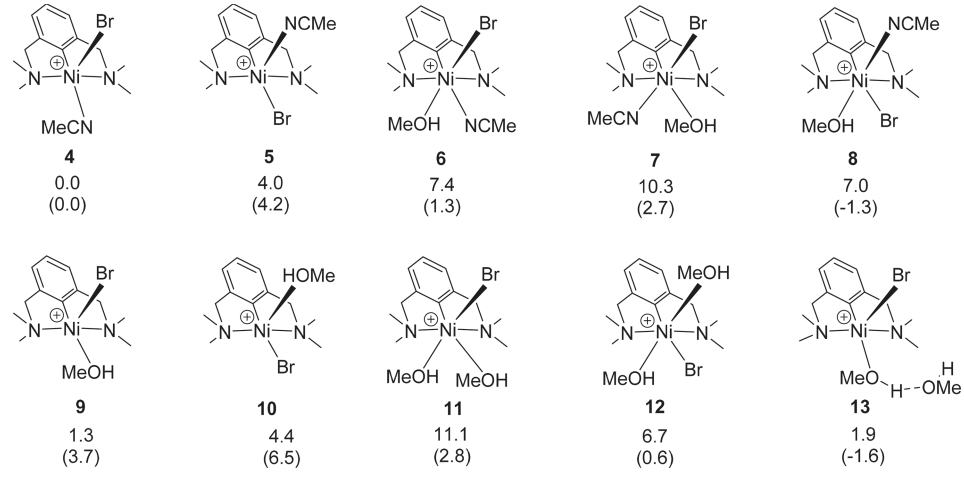

of the $d_{x^2-y^2}$ orbital and interacts in an antibonding fashion with the p_x orbitals of the nitrogen atoms, as well as with the p_y orbital from the axial acetonitrile's lone pair. The α-HOMO−2 is a mixture between the d_{xz} and the amine lone pairs of the pincer ligand. The two last α-spin metal-based orbitals, located at ∼2.0 eV from the α-HOMO, are the d_{yz} and the d_{xy}, both of which are involved in an antibonding interaction with the 3 acetonitrile ligands. The β-spin manifold contains 3 orbitals of metal character (96, 95, and 93) for a total of 7 d electrons.

DFT Analysis of the Mechanism for Reactions of 3 and 4 with CH_3OH. Scheme 8 shows a simplified mechanistic proposal for C−O functionalization of the Ni-aryl moiety in **4**

DOI: 10.1021/acs.inorgchem.8b03489
Inorg. Chem. 2019, 58, 3861−3874

Scheme 10. (a) Lowest Free Energy (and Enthalpy) Landscape for Reaction of 4 with CH_3OH and (b) Representative Examples of Higher-Energy Transition States Examined (kcal/mol)

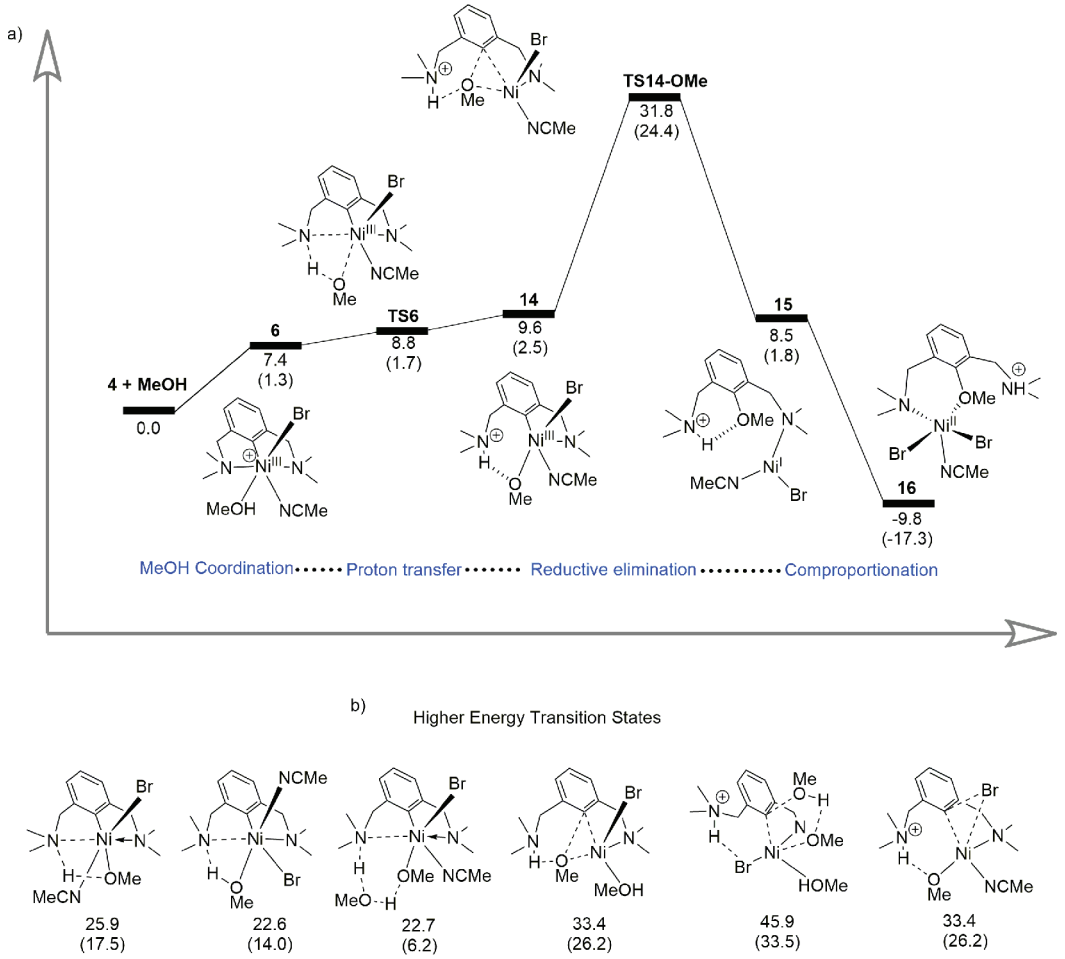

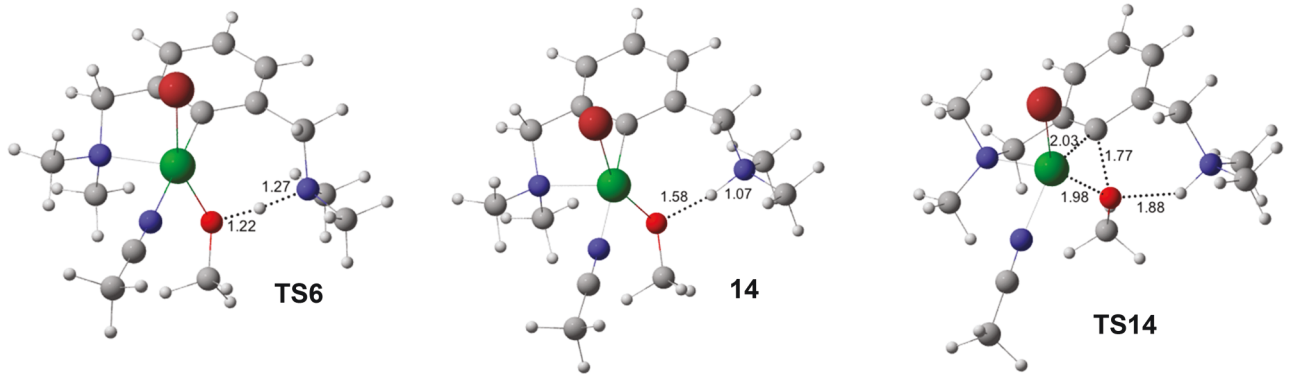

Figure 9. 3D representations of proton transfer and reductive elimination transitions states for the reaction of **4** with CH_3OH. Bond and partial bond lengths are reported in angstroms.

involving the following elementary steps: (i) CH_3OH coordination, (ii) proton transfer to the NMe_2 side arm of the pincer ligand, and (iii) formation of C−O bond through reductive elimination.

We began by calculating the relative free energies and enthalpies for possible CH_3OH coordination complexes and ligand substitution; as expected, there are a large variety of low-energy complexes (Scheme 9). The hexa-coordinate complex **6** shows that CH_3OH coordination is unfavorable: it is indeed endothermic and endergonic by 1.3 and 7.4 kcal/mol, respectively. The unfavorable coordination of methanol is likely the result of the α-spin HOMO occupation shown in Figure 7; because this MO is antibonding in character, the dative Ni−O coordination interaction is destabilizing. This is confirmed by a relatively long Ni−O(CH_3)H distance of 2.17 Å in **6**. Next, the positional isomer represented by structure **8** (wherein Br and CH_3CN have switched positions) appears slightly more stable than **6**, but the **4** → **8** conversion is still uphill in free energy. Overall, these calculated structures confirm that acetonitrile is easily replaced by CH_3OH. For

DOI: 10.1021/acs.inorgchem.8b03489
Inorg. Chem. 2019, 58, 3861−3874

example, structure **9** is only 1.3 kcal/mol endergonic relative to **4**.

We then performed a comprehensive search for the CH_3OH-to-$NMe_{2(ligand)}$ proton transfer from all of the identified ground states. The lowest-energy pathway identified involves starting from ground-state **6** and proceeds through transition-state structure **TS6** (Scheme 10a). The energy surface of this proton transfer is extremely flat and endothermic/endergonic, and while the resulting intermediate **14** is a potential surface minimum, it is slightly higher in free energy compared to **TS6**. The 3D structure of **TS6** shows that the Ni-NMe_2 coordination is completely severed prior to proton transfer (Figure 9). Direct deprotonation from adducts **7** and **8** showed transition states located ∼22−26 kcal/mol higher than the starting complex **4**. This last observation indicates that deprotonation is less favorable when CH_3OH is *trans* to the phenyl ring or to the MeCN ligand.

We also examined the possibility that another CH_3OH might serve as a shuttle for the CH_3OH-to-$NMe_{2(ligand)}$ proton transfer (Scheme 10b, third species from the left). This transition state is ∼5 kcal/mol higher in enthalpy than **TS6**; in addition, such CH_3OH proton shuttling is likely also disfavored by the entropy penalty.[17] Interestingly, protonation of the aryl moiety by CH_3OH to generate a demetalated Ni^{III} alkoxy complex was found to be thermodynamically unfavorable by 29 kcal/mol (Scheme 11). This suggests that the

Scheme 11. Possible Protonation of the Aryl Moiety by CH_3OH

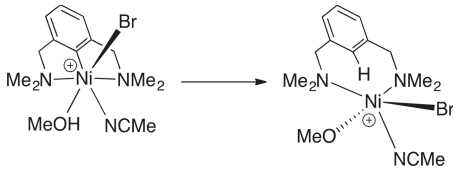

reverse reaction, C−H activation, should be thermodynamically feasible; indeed, examples of high-valent nickel-promoted C−H activation have been observed by Mirica and Sanford.[18]

Subsequent to the proton transfer, the aryl moiety of the pincer ligand and the methoxide group are *cis* to each other and thus primed for C−O bond-forming reductive elimination. Examination of reductive elimination from a variety of ground states allowed us to identify **TS14** as lowest in energy (see the Supporting Information for alternative transition states). The barrier from **14** to **TS14** is 22.2 kcal/mol (Scheme 10a) and overall 31.8 kcal/mol relative to **4** and CH_3OH. This large free energy value is most likely due to entropy overestimation; the enthalpy of activation is 24.4 kcal/mol, which is more reasonable for a room-temperature reaction. The reductive elimination transition states leading to C−Br bond formation were also located, but the barriers for these are 2−5 kcal/mol higher in energy relative to **TS14**, which is just enough to disfavor formation of the C−Br coupling product NC(Br)N.

As an alternative to the proposed inner-sphere, cis-reductive elimination, we also investigated the possibility of direct nucleophilic attack by CH_3OH on the *ipso*-C *atom* (transition state depicted in Scheme 10b, the second-to-last drawing from the right). This transition state turned out to have a barrier of over 45 kcal/mol, indicating that it is not competitive with intramolecular reductive elimination. Somewhat unexpectedly, the C−O coupling that generates the Ni^{I} species **15** via **TS14** is endergonic by 8.5 kcal/mol (Scheme 10a). This finding prompted us to examine the possibility that **15** reacts with **4** to generate **16** and **1**. Indeed, this reaction provides an overall exergonic reaction by ∼10 kcal/mol. An analogous reaction between the NC(Br)N product of the bromide reductive elimination and **4** does not serve to make the process exergonic.

Given the experimentally measured Ni^{III}/Ni^{IV} oxidation potential of **4** (0.74 V), it seems rather unlikely that Ni^{IV} species might form during the functionalization reactions of this complex in the absence of external oxidants. Nonetheless, it is possible to envisage that some of the more electron-rich intermediates of the reaction (e.g., the Ni^{III}−OCH_3 generated by the deprotonation of the CH_3OH adduct) might be oxidized to a Ni^{IV} species in a disproportionation reaction, as outlined in Scheme 12. Our calculations showed, however, that the free energy of this reaction is 34.2 kcal/mol with respect to **4** + CH_3OH, which suggests a mechanism far too high in energy to be viable.

In the case of the coordinatively saturated, 19-electron dicationic species **3**, the reaction needs to go through MeCN dissociation first before CH_3OH can bind to the metal center (Scheme 13). Interestingly, dissociation of MeCN is exergonic by ca. 7 kcal/mol, while CH_3OH binding is slightly uphill; overall, the new adduct **18** thus generated is more stable than the starting material **3**. The deprotonation of coordinated CH_3OH appears to be endergonic, but all attempts failed to locate a transition state for the direct deprotonation by the NMe_2 moiety. On the other hand, our calculations revealed that reductive elimination from the putative Ni-OCH_3 intermediate, species **19**, is relatively facile with an activation barrier of 17.0 kcal/mol (Scheme 13), which is much lower than the corresponding step in the reaction of CH_3OH with the monocationic complex **4** (ca. 31.8 kcal/mol). Moreover, **TS19** (Figure 10) connects to product **20** located 5.1 kcal/mol lower than the starting material. The comproportionation reaction with **3** brings the Gibbs energy of the whole process to −27.7 kcal/mol.

Kinetic Isotope Effect Calculation. The energy landscape shown in Scheme 10a provides an understanding of the observed inverse kinetic isotope value of 0.62 obtained experimentally for the functionalization of **4** with CH_3OH/CD_3OD. The key feature of the energy surface is that the proton transfer is an endothermic step prior to the rate-limiting reductive elimination transition state. This suggested to us that the inverse KIE based on k_{obs} results from an inverse

Scheme 12. Possible Disproportionation Reaction between Two Ni^{III} Complexes

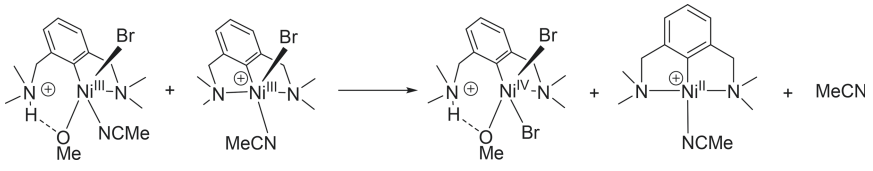

DOI: 10.1021/acs.inorgchem.8b03489
Inorg. Chem. 2019, 58, 3861−3874

Scheme 13. Lowest Free Energy Landscape (and Enthalpies) for Reaction of 3 with CH_3OH

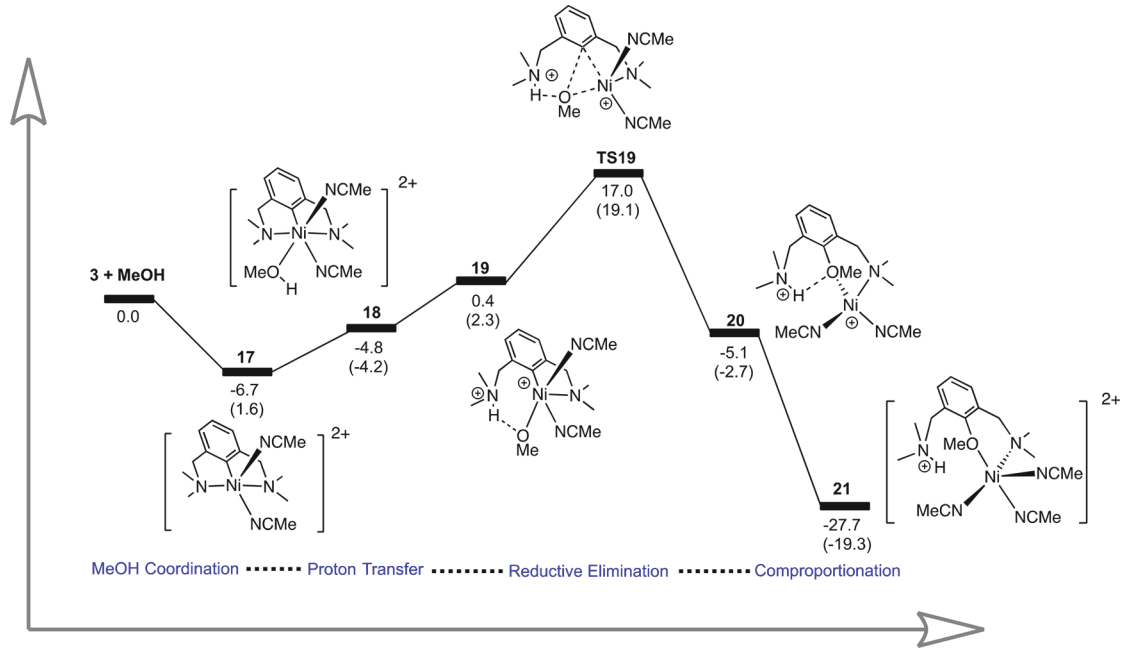

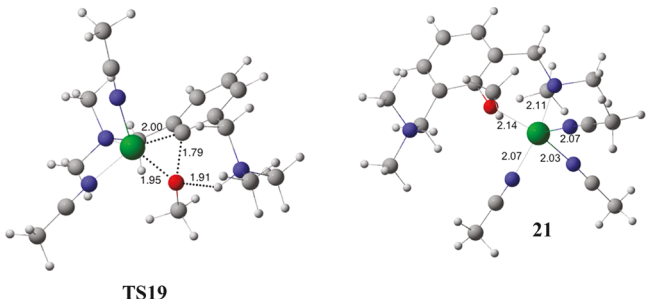

Figure 10. 3D representations of reductive elimination transition state and final product for the reaction of **3** with CH_3OH. Bond and partial bond lengths are reported in angstroms.

equilibrium isotope effect (EIE). While there are several contributing components to a KIE/EIE, including symmetry factor, mass moment of inertia factor, vibrational excitation, and zero-point energy (ZPE), we have modeled only the ZPE component.

As expected, the proton-transfer step (**TS6**, Scheme 10a) shows normal KIE of about 3.4 with respect to **6**, because the O−H bond is breaking. However, because this transition state is prior to the rate-limiting transition state and the intermediate resulting from this transition state is endothermic, the KIE value of this step does not significantly impact the overall observed KIE value. The steps that will impact the observed KIE are the CH_3OH coordination equilibrium and the rate-limiting reductive elimination. The calculated k_H/k_D value for **TS14** relative to **4** and CH_3OH/CD_3OD is 0.57. This overall inverse KIE value results from an inverse KIE value for reaction step **14** to **TS14** and an inverse EIE value for conversion of **4** to **6**. The predicted KIE value for **14** → **TS14** is 0.67, whereas the predicted EIE for **4** → **6** is 0.76. This inverse EIE is likely the result of additional vibrational modes formed when CH_3OH coordinates to the Ni metal center. In accordance with this notion, inspection of the stretching vibrational modes for free CH_3OH/CD_3OD shows a difference of ∼3500 cm^{-1}, which is very similar to the difference in stretching modes for **6** and its isotopologue. However, consideration of lower-frequency modes such as bending, wagging, and rocking, as well as new isotope-sensitive modes due to substrate coordination, leads to a preference for the coordination of CD_3OD over CH_3OH, thus leading to an inverse EIE. Parkin, Bender, and Goldman made similar arguments in rationalizing the observed inverse EIE's for the coordination and oxidative addition of H_2/D_2 to iridium and tungsten metal centers.[19]

C−N Functionalization of the Monocationic and Dicationic Species 4 and 3 with CH_3NH_2. The energy landscape for the reaction of **4** with CH_3NH_2 is shown in Scheme 14a. Coordination of CH_3NH_2 to the Ni^{III} center in **4** was found to be exothermic by 4.7 kcal/mol and endergonic by 2.8 kcal/mol. Unlike in the case of the CH_3OH reactions discussed above, we did not succeed in locating a transition state for the direct deprotonation of coordinated CH_3NH_2 by the NMe_2 arm of the pincer ligand. Therefore, we elected to consider the alternative scenario of an outer-sphere deprotonation mechanism wherein a second molecule of CH_3NH_2 would act as a deprotonating agent. The transition state for this type of deprotonation was located at 19.5 kcal/mol (**TS22**), and the deprotonated species **23** is 20.2 kcal/mol above **4**. Release of $CH_3NH_3^+$ from **23** leads to the charge-neutral, 19-electron Ni^{III} amide complex **24** (Figure 11) from which C−N or C−Br bond formation can occur. As was the case in the CH_3OH reaction, our calculations showed that C−Br reductive elimination is disfavored kinetically, whereas C−N bond formation is much more favorable kinetically (activation energy, ∼30 kcal/mol).

The analogous backbone functionalization starting from the dicationic complex **3** and CH_3NH_2 starts with MeCN dissociation to form the penta-coordinated species **17** (Scheme 15a), followed by exothermic/exergonic substrate uptake to generate the CH_3NH_2 adduct **26**. It is significant that substitution of MeCN by the substrate is thermodynamically favored (by −10.4 kcal/mol) and that even the deprotonation

DOI: 10.1021/acs.inorgchem.8b03489
Inorg. Chem. 2019, 58, 3861−3874

Scheme 14. (a) Lowest Free Energy (and Enthalpy) Landscape for the Reaction of 4 with CH_3NH_2 and (b) Representative Example of the Higher-Energy Transition States Examined (kcal/mol)

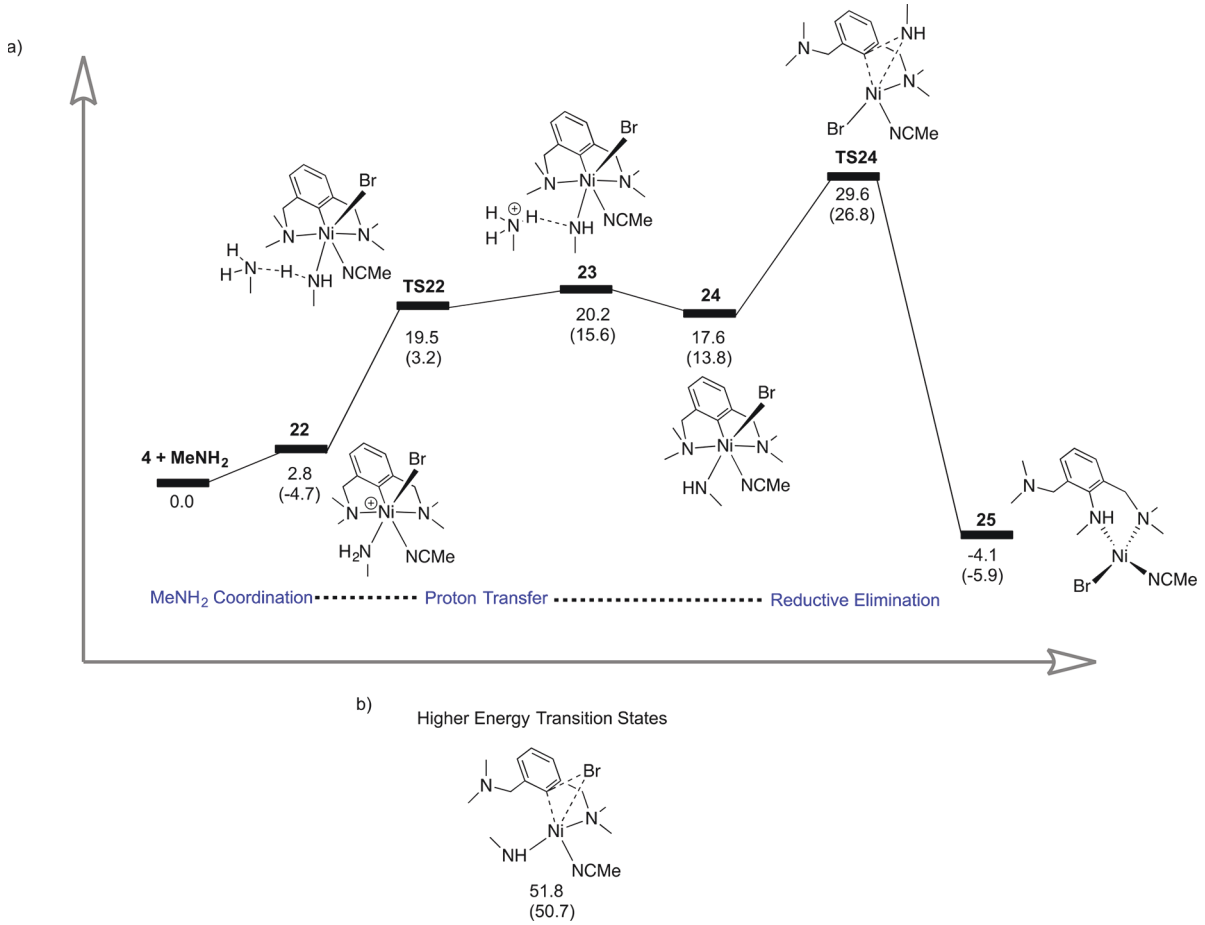

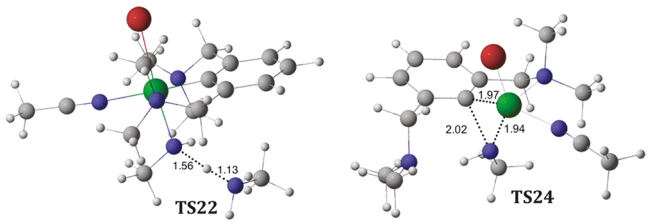

Figure 11. 3D representations of proton transfer and reductive elimination transition states for the reaction of **4** with CH_3NH_2. Bond and partial bond lengths are reported in angstroms.

of coordinated CH_3NH_2 proceeds rather easily via an outer sphere mechanism, i.e., mediated by a second molecule of substrate (<4 kcal/mol). Thus, C−N reductive elimination is rate-determining with a relatively accessible transition state **TS28** at 9.6 kcal/mol (Figure 12). It is worth noting that a slightly greater activation energy (10.5 kcal/mol) was required for an alternative pathway involving the disruption of the chelating form of the pincer ligand. Much like CH_3NH_2 functionalization from **4**, this mechanism does not require comproportionation with starting material to be favorable thermodynamically.

CONCLUSIONS

This work has resulted in the synthesis and characterization of the new divalent and trivalent cationic Ni complexes **1**, **3**, and **4**, as well as an examination of their reactivities toward protic substrates. The divalent complex **1** was found to undergo a sluggish functionalization of its Ni^{II}−Ar moiety with CH_3OH; this reactivity requires aerobic conditions and in this sense is reminiscent of the previously reported C−O and C−N bond formation from pyrazole-based NCN-type pincer complexes isolated by our group.[5] These observations hint at the involvement of cationic Ni^{III} intermediates. The successful isolation and characterization of monocationic and dicationic Ni^{III} complexes discussed in this report allowed us to confirm the viability of this hypothesis. Furthermore, we have established that several side reactions diminish the yield of backbone functionalization. For instance, a comproportionation reaction between in situ generated Ni^{I} species and the Ni^{III} precursors limits to 50% the conversion of the mono- and dicationic trivalent species **3** and **4** into the functionalization product $NC(OCH_3)N$. This undesirable side reaction can, however, be circumvented by performing the reaction under aerobic conditions, because the in situ generated divalent complex **1** can, in turn, undergo C−O coupling thereby improving the overall coupling yield. It should be noted, however, that aerobic reaction conditions did not lead to substantial increases in C−N coupling yields. Finally, another side reaction is the rapid oxidation of amines by the cationic Ni^{III} complexes; this side reaction also forms the cationic Ni^{II} complex **1**.

DFT calculations revealed a number of valuable observations. Substrate uptake by the nickel center is surprisingly difficult, especially in the case of the monocationic complex **4**;

DOI: 10.1021/acs.inorgchem.8b03489
Inorg. Chem. 2019, 58, 3861−3874

Scheme 15. (a) Lowest Free Energy (and Enthalpy) Landscape for Reaction of 3 with CH_3NH_2 and (b) Representative Example of the Higher-Energy Transitions States Examined (kcal/mol)

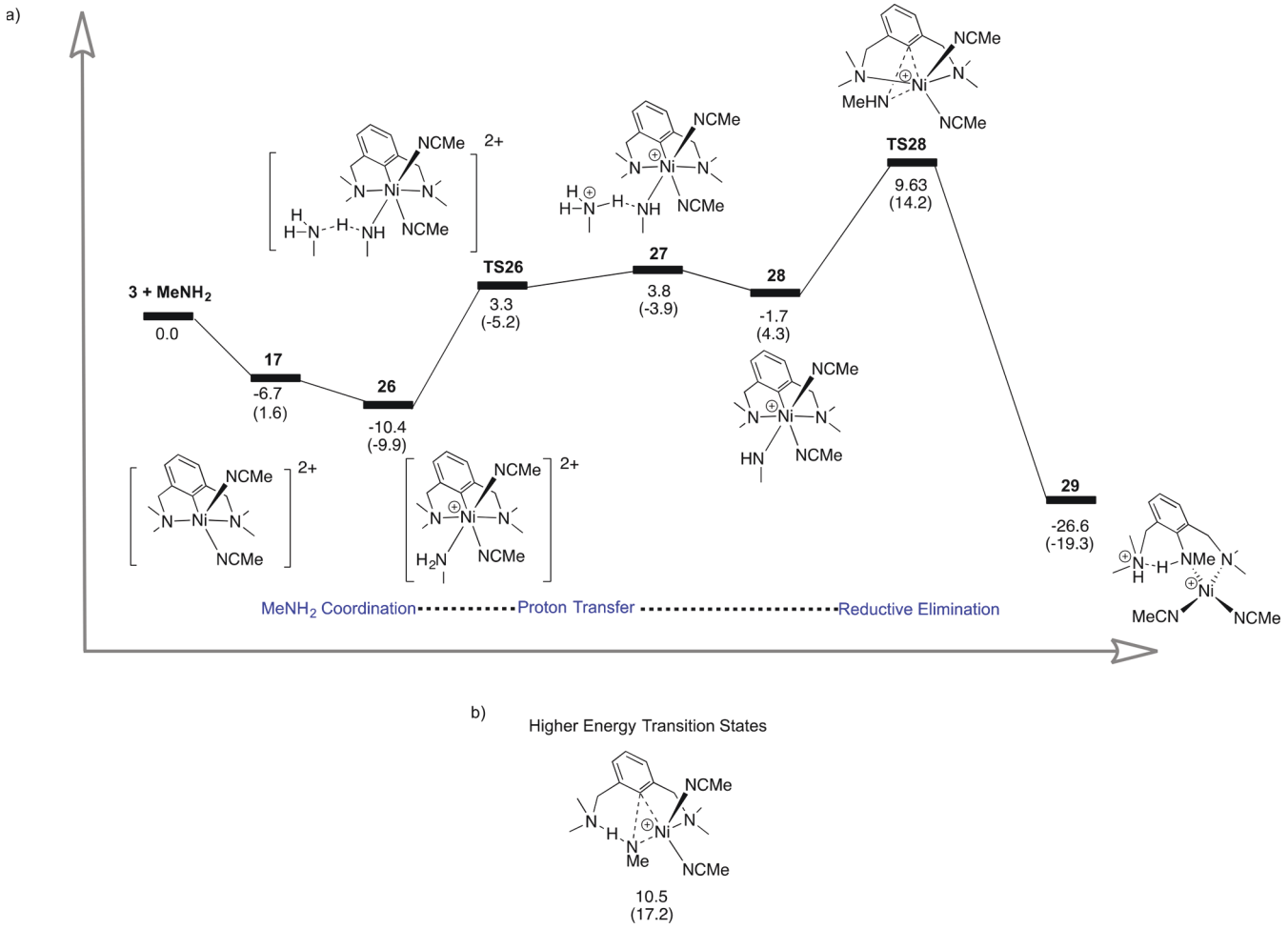

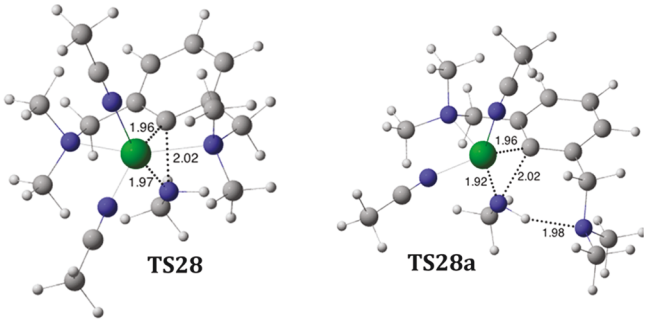

Figure 12. 3D representations of reductive elimination transition states for the reaction of **3** and CH_3NH_2. Bond and partial bond lengths are reported in angstroms.

however, once coordination takes place, the requisite deprotonation is fast. Reductive elimination of the methoxy and amide ligand is favored compared to C−Br bond formation, both kinetically and thermodynamically. This suggests that the reverse reaction, oxidative addition, should be accessible from Ni^{I} and that one could devise a Ni^{I}/Ni^{III} catalytic cycle for the conversion of C−Br bonds into C−O bonds.[20] Moreover, the fact that protonation of the aryl moiety is thermodynamically disfavored suggests that electrophilic type C−H activation of a pincer ligand from a Ni^{III} complex should be possible. Future investigations will explore these two avenues.

EXPERIMENTAL SECTION

General Procedures. Unless otherwise indicated, all manipulations were carried out using standard Schlenk and glovebox techniques under a dry nitrogen atmosphere and using solvents which were dried to water content of less than 10 ppm by passage through activated aluminum oxide columns (MBraun SPS); solvent moisture content was determined using a Mettler-Toledo C20 coulometric Karl Fischer titrator. The starting materials $AgSBF_6$, 3,5-dimethoxybromophenol, $CuBr_2$, and CD_3OD were purchased from Aldrich and used without further purification. Literature procedures were used to synthesize $NiBr_2(NCiPr)$,[21] NC(H)N,[22] and $(NCN)NiBr_2$.[7]

The NMR spectra were recorded on the following spectrometers: Bruker AV400rg (^1H at 400 MHz) and Bruker ARX400 (^1H at 400 MHz and $^{13}C\{^1H\}$ at 100.56 MHz). Chemical shift values are reported in ppm (δ) and referenced internally to the residual solvent signals (^1H and ^{13}C: 7.16 and 128.06 ppm for C_6D_6) or externally. Coupling constants are reported in Hz. The elemental analyses were performed by the Laboratoire d'Analyses Élémentaires, Département de chimie, Université de Montréal. The EPR spectra were collected on a Bruker Elexys E500 X-band spectrometer. The samples were prepared by dissolving under an inert atmosphere the Ni(III) complex **3** or **4** (0.1 mM) with a dry solvent (MeCN for **3** and MeCN/toluene or CH_2Cl_2/toluene for **4**) in a 4 mm EPR tube. Measurements were

DOI: 10.1021/acs.inorgchem.8b03489
Inorg. Chem. 2019, 58, 3861−3874

then carried out either in a liquid (293 K) or in a frozen solution (120 K).

[(NCN)Ni^{III}(MeCN)$_3$][SbF$_6$]$_2$, **3**. A dry Schlenk flask was charged with MeCN (15 mL), the charge-neutral dibromo precursor (NCN)-Ni^{III}Br$_2$, **2** (0.400 g, 0.976 mmol), and $AgSbF_6$ (0.671 g, 1.95 mmol). The flask was wrapped in aluminum foil, and the suspension was stirred for 30 min at r.t. The final reaction mixture was concentrated under vacuum to ∼4 mL, followed by addition of Et_2O (15 mL) and filtration to isolate a red precipitate, which was then washed with 3 × 10 mL of Et_2O to give a red powder (0.684 g, 84% yield). Anal. Calc for $C_{18}H_{28}F_{12}N_5NiSb_2$ (844.64): C, 25.60; N, 8.12; H, 3.34. Found: C, 25.10; N, 8.27; H, 3.38.

[(NCN)Ni^{III}(Br)(MeCN)][SbF$_6$], **4**. A dry Schlenk flask was charged with MeCN (5 mL), the dicationic complex **3** (0.150 g, 0,178 mmol), and the charge-neutral dibromo precursor (NCN)Ni^{III}Br$_2$, **2** (0.080 g, 0.196 mmol). The reaction mixture was stirred at r.t. for 20 min, followed by concentration of the resulting purple solution to ∼1 mL. Addition of Et_2O (10 mL) and canula filtration, followed by washing of the residual solid with 5 × 10 mL of Et_2O, gave a purple powder (0.170 g, 83% yield). Anal. Calc for $C_{14}H_{22}N_3F_6BrNiSb$ (606.96): C, 27.72; N, 6.93; H, 3.66. Found: C, 27.59; N, 6.92; H, 3.53.

■ ASSOCIATED CONTENT

Supporting Information

The Supporting Information is available free of charge on the ACS Publications website at DOI: 10.1021/acs.inorgchem.8b03489.

NMR Data, yield determination procedures, kinetic data, DFT data, and reaction schemes (PDF)

Accession Codes

CCDC 1876860−1876862 contain the supplementary crystallographic data for this paper. These data can be obtained free of charge via www.ccdc.cam.ac.uk/data_request/cif, or by emailing data_request@ccdc.cam.ac.uk, or by contacting The Cambridge Crystallographic Data Centre, 12 Union Road, Cambridge CB2 1EZ, UK; fax: +44 1223 336033.

■ AUTHOR INFORMATION

Corresponding Authors

*E-mail: zargarian.davit@umontreal.ca.
*E-mail: dhe@chem.byu.edu.

ORCID

Yves Canac: 0000-0002-3747-554X
Daniel H. Ess: 0000-0001-5689-9762
Davit Zargarian: 0000-0002-0207-7007

Notes

The authors declare no competing financial interest.

■ ACKNOWLEDGMENTS

The authors gratefully thank the Office of Research Computing at BYU and the Fulton Supercomputing Lab. D.H.E. thanks the United States National Science Foundation Chemical Catalysis Program for support (CHE-1764194). Y.C. thanks the Centre National de la Recherche Scientifique (CNRS, France) for financial support. D.Z. is grateful to NSERC (Canada) for continued support of his group's research program on high-valent nickel chemistry. J.P.C. thanks the department of Chemistry, Université de Montréal, for a Denis Gravel scholarship and other teaching fellowships.

■ REFERENCES

(1) (a) Terrett, J. A.; Cuthbertson, J. D.; Shurtleff, V. W.; MacMillan, D. W. Switching on Elusive Organometallic Mechanisms with Photoredox Catalysis. *Nature* **2015**, *524* (7565), 330−334. (b) Lim, C.-H.; Kudisch, M.; Liu, B.; Miyake, G. M. C−N Cross-Coupling via Photoexcitation of Nickel−Amine Complexes. *J. Am. Chem. Soc.* **2018**, *140* (24), 7667−7673. (c) Martinez, G. E.; Nugent, J. W.; Fout, A. R. Simple Nickel Salts for the Amination of (Hetero)Aryl Bromides and Iodides with Lithium Bis(Trimethylsilyl)-Amide. *Organometallics* **2018**, *37*, 2941. (d) Green, R. A.; Hartwig, J. F. Nickel-Catalyzed Amination of Aryl Chlorides with Ammonia or Ammonium Salts. *Angew. Chem., Int. Ed.* **2015**, *54* (12), 3768−3772. (e) Borzenko, A.; Rotta Loria, N. L.; MacQueen, P. M.; Lavoie, C. M.; McDonald, R.; Stradiotto, M. Nickel-Catalyzed Monoarylation of Ammonia. *Angew. Chem., Int. Ed.* **2015**, *54* (12), 3773−3777.

(2) (a) Koo, K.; Hillhouse, G. L. Carbon-Nitrogen Bond Formation by Reductive Elimination from Nickel(II) Amido Alkyl Complexes. *Organometallics* **1995**, *14* (9), 4421−4423. (b) Han, R.; Hillhouse, G. L. Carbon−Oxygen Reductive-Elimination from Nickel(II) Oxametallacycles and Factors That Control Formation of Ether, Aldehyde, Alcohol, or Ester Products. *J. Am. Chem. Soc.* **1997**, *119* (34), 8135−8136. (c) Lin, B. L.; Clough, C. R.; Hillhouse, G. L. Interactions of Aziridines with Nickel Complexes: Oxidative-Addition and Reductive-Elimination Reactions That Break and Make C−N Bonds. *J. Am. Chem. Soc.* **2002**, *124* (12), 2890−2891.

(3) (a) Zhou, W.; Schultz, J. W.; Rath, N. P.; Mirica, L. M. Aromatic Methoxylation and Hydroxylation by Organometallic High-Valent Nickel Complexes. *J. Am. Chem. Soc.* **2015**, *137* (24), 7604−7607. (b) Zhou, W.; Rath, N. P.; Mirica, L. M. Oxidatively-Induced Aromatic Cyanation Mediated by Ni(III). *Dalton Trans.* **2016**, *45* (21), 8693−8695. (c) Zhou, W.; Watson, M. B.; Zheng, S.; Rath, N. P.; Mirica, L. M. Ligand Effects on the Properties of Ni(III) Complexes: Aerobically-Induced Aromatic Cyanation at Room Temperature. *Dalton Trans.* **2016**, *45* (40), 15886−15893.

(4) (a) Camasso, N. M.; Sanford, M. S. Design, Synthesis, and Carbon-Heteroatom Coupling Reactions of Organometallic Nickel-(IV) Complexes. *Science* **2015**, *347* (6227), 1218−1220. (b) D'Accriscio, F.; Borja, P.; Saffon-Merceron, N.; Fustier-Boutignon, M.; Mezailles, N.; Nebra, N. C-H Bond Trifluoromethylation of Arenes Enabled by a Robust, High-Valent Nickel(IV) Complex. *Angew. Chem., Int. Ed.* **2017**, *56* (42), 12898−12902.

(5) Cloutier, J.-P.; Vabre, B.; Moungang-Soumé, B.; Zargarian, D. Synthesis and Reactivities of New NCN-Type Pincer Complexes of Nickel. *Organometallics* **2015**, *34* (1), 133−145.

(6) Cloutier, J.-P.; Zargarian, D. Functionalization of the Aryl Moiety in the Pincer Complex (NCN)Ni^{III}Br$_2$: Insights on Ni^{III}-Promoted Carbon−Heteroatom Coupling. *Organometallics* **2018**, *37* (9), 1446−1455.

(7) This trivalent complex was introduced over three decades ago by van Koten's group: Grove, D. M.; Van Koten, G.; Zoet, R.; Murrall, N. W.; Welch, A. J. Unique Stable Organometallic Nickel(III) Complexes; Syntheses and the Molecular Structure of [Ni-[C$_6$H$_3$(CH$_2$NMe$_2$)2−2,6]I$_2$]. *J. Am. Chem. Soc.* **1983**, *105* (5), 1379−1380.

(8) Grove, D. M.; Van Koten, G.; Ubbels, H. J. C.; Zoet, R.; Spek, A. L. Organonickel(II) Complexes of the Tridentate Monoanionic Ligand o,o'-Bis[(Dimethylamino)Methylphenyl (N-C-N). Syntheses and the x-Ray Crystal Structure of the Stable Nickel(II) Formate [Ni(N-C-N)O$_2$CH]. *Organometallics* **1984**, *3* (7), 1003−1009.

(9) (a) Baho, N.; Zargarian, D. Syntheses, Structures, Spectroscopy, and Chromotropism of New Complexes Arising from the Reaction of Nickel(II) Nitrate with Diphenyl(Dipyrazolyl)Methane. *Inorg. Chem.* **2007**, *46* (1), 299−308. (b) Lapointe, S.; Vabre, B.; Zargarian, D. POCOP-Type Pincer Complexes of Nickel: Synthesis, Characterization, and Ligand Exchange Reactivities of New Cationic Acetonitrile Adducts. *Organometallics* **2015**, *34* (14), 3520−3531. (c) Lefèvre, X.; Spasyuk, D. M.; Zargarian, D. New POCOP-Type Pincer Complexes of Nickel(II). *J. Organomet. Chem.* **2011**, *696* (4), 864−870. (d) Wang, R.; Groux, L. F.; Zargarian, D. Nickel-Triflate Complexes as Precursors to Reactive Cations: Preparation and Reactivities of (1-R-Indenyl)Ni(PPh$_3$)(OSO$_2$CF$_3$). *Organometallics* **2002**, *21* (25), 5531−5539. (e) Spasyuk, D. M.; Gorelsky, S. I.; van

DOI: 10.1021/acs.inorgchem.8b03489
Inorg. Chem. 2019, 58, 3861−3874

der Est, A.; Zargarian, D. Characterization of Divalent and Trivalent Species Generated in the Chemical and Electrochemical Oxidation of a Dimeric Pincer Complex of Nickel. *Inorg. Chem.* **2011**, *50* (6), 2661−2674. (f) Groux, L. F.; Zargarian, D. Aminoalkyl-Substituted Indenyl−Nickel Compounds: Tuning Reactivities as a Function of the Pendant, Hemilabile Moiety. *Organometallics* **2003**, *22* (15), 3124−3133.

(10) For example, the Ni−N_{NCMe} distances in **3** are longer by ca. 16 esd in the axial positions than in the equatorial plane; this is attributed to the partial antibonding character of the axial interactions involving the singly occupied d_{z^2} orbital.

(11) Grove, D. M.; Van Koten, G.; Mul, P.; Van der Zeijden, A. A. H.; Terheijden, J.; Zoutberg, M. C.; Stam, C. H. Arylnickel(III) Species Containing Nitrogen Trioxide, Nitrogen Dioxide, and Thiocyanate Ligands. ESR Data and the x-Ray Crystal Structure of Hexacoordinate (Pyridine)Bis(Thiocyanato)[o,o'-Bis-{(Dimethylamino)Methyl}phenyl]Nickel(III). *Organometallics* **1986**, *5* (2), 322−326.

(12) Stol, M.; Snelders, D. J. M.; Godbole, M. D.; Havenith, R. W. A.; Haddleton, D.; Clarkson, G.; Lutz, M.; Spek, A. L.; van Klink, G. P. M.; van Koten, G. 2,6-Bis(Oxazolinyl)Phenylnickel(II) Bromide and 2,6-Bis(Ketimine)Phenylnickel(II) Bromide: Synthesis, Structural Features, and Redox Properties. *Organometallics* **2007**, *26* (16), 3985−3994.

(13) Lin, W.; Bodenstein, T.; Mereacre, V.; Fink, K.; Eichhofer, A. Field-Induced Slow Magnetic Relaxation in the Ni(I) Complexes $[NiCl(PPh_3)_2].C_4H_8O$ and $[Ni(N(SiMe_3)_2)(PPh_3)_2]$. *Inorg. Chem.* **2016**, *55* (5), 2091−2100.

(14) Amine oxidation by ferrocenium is reported in the literature, see: Torriero, A. A. J.; Shiddiky, M. J. A.; Burgar, I.; Bond, A. M. Homogeneous Electron-Transfer Reaction between Electrochemically Generated Ferrocenium Ions and Amine-Containing Compounds. *Organometallics* **2013**, *32* (20), 5731−5739.

(15) Frisch, M. J.; Trucks, G. W.; Schlegel, H. B.; Scuseria, G. E.; Robb, M. A.; Cheeseman, J. R.; Scalmani, G.; Barone, V.; Mennucci, B.; Petersson, G. A.; Nakatsuji, H.; Caricato, M.; Li, X.; Hratchian, H. P.; Izmaylov, A. F.; Bloino, J.; Zheng, G.; Sonnenberg, J. L.; Hada, M.; Ehara, M.; Toyota, K.; Fukuda, R.; Hasegawa, J.; Ishida, M.; Nakajima, T.; Honda, Y.; Kitao, O.; Nakai, H.; Vreven, T.; Montgomery, J. A., Jr.; Peralta, J. E.; Ogliaro, F.; Bearpark, M.; Heyd, J. J.; Brothers, E.; Kudin, K. N.; Staroverov, V. N.; Kobayashi, R.; Normand, J.; Raghavachari, K.; Rendell, A.; Burant, J. C.; Iyengar, S. S.; Tomasi, J.; Cossi, M.; Rega, N.; Millam, J. M.; Klene, M.; Knox, J. E.; Cross, J. B.; Bakken, V.; Adamo, C.; Jaramillo, J.; Gomperts, R.; Stratmann, R. E.; Yazyev, O.; Austin, A. J.; Cammi, R.; Pomelli, C.; Ochterski, J. W.; Martin, R. L.; Morokuma, K.; Zakrzewski, V. G.; Voth, G. A.; Salvador, P.; Dannenberg, J. J.; Dapprich, S.; Daniels, A. D.; Farkas, O.; Foresman, J. B.; Ortiz, J. V.; Cioslowski, J.; Fox, D. J. *Gaussian 09*, revision B.01; Gaussian, Inc.: Wallingford, CT, 2009.

(16) For M06-L see: (a) Zhao, Y.; Truhlar, D. G. A new local density functional for main-group thermochemistry, transition metal bonding, thermochemical kinetics, and noncovalent interactions. *J. Chem. Phys.* **2006**, *125*, No. 194101. (b) Zhao, Y.; Truhlar, D. G. Density Functionals with Broad Applicability in Chemistry. *Acc. Chem. Res.* **2008**, *41*, 157. (c) Zhao, Y.; Truhlar, D. The M06 suite of density functionals for main group thermochemistry, thermochemical kinetics, noncovalent interactions, excited states, and transition elements: two new functionals and systematic testing of four M06-class functionals and 12 other functionals. *Theor. Chem. Acc.* **2008**, *120*, 215. For basis sets, see: (d) Hay, P. J.; Wadt, W. R. Ab initio effective core potentials for molecular calculations. Potentials for the transition metal atoms Sc to Hg. *J. Chem. Phys.* **1985**, *82*, 270. (e) Weigend, F.; Ahlrichs, R. Balanced basis sets of split valence, triple zeta valence and quadruple zeta valence quality for H to Rn: Design and assessment of accuracy. *Phys. Chem. Chem. Phys.* **2005**, *7*, 3297. For the SMD model see: (f) Marenich, A. V.; Cramer, C. J.; Truhlar, D. G. Universal solvation model based on solute electron density and on a continuum model of the solvent defined by the bulk dielectric constant and atomic surface tensions. *J. Phys. Chem. B* **2009**, *113*, 6378.

(17) We did not calculate the proton shuttle pathway for **8** for the following reason: the adduct **8**(MeOH) corresponding to complex **8** with another MeOH in the second coordination sphere is located 8.94 kcal/mol above reactants, which is already higher than **TS6**.

(18) (a) Chong, E.; Kampf, J. W.; Ariafard, A.; Canty, A. J.; Sanford, M. S. Oxidatively Induced C-H Activation at High Valent Nickel. *J. Am. Chem. Soc.* **2017**, *139* (17), 6058−6061. (b) Zhou, W.; Zheng, S.; Schultz, J. W.; Rath, N. P.; Mirica, L. M. Aromatic Cyanoalkylation through Double C-H Activation Mediated by Ni(III). *J. Am. Chem. Soc.* **2016**, *138* (18), 5777−5780.

(19) (a) Hascall, T.; Rabinovich, D.; Murphy, V. J.; Beachy, M. D.; Friesner, R. A.; Parkin, G. Mechanistic and Theoretical Analysis of the Oxidative Addition of H2 to Six-Coordinate Molybdenum and Tungsten Complexes $M(PMe_3)_4X_2$ (M = Mo, W; X = F, Cl, Br, I): An Inverse Equilibrium Isotope Effect and an Unprecedented Halide Dependence. *J. Am. Chem. Soc.* **1999**, *121* (49), 11402−11417. (b) Abu-Hasanayn, F.; Krogh-Jespersen, K.; Goldman, A. S. Theoretical Study of Primary and Secondary Deuterium Equilibrium Isotope Effects for Hydrogen and Methane Addition to Iridium Complex Trans-$Ir(PR_3)2(CO)_X$. *J. Am. Chem. Soc.* **1993**, *115* (18), 8019−8023. (c) Bender, B. R.; Kubas, G. J.; Jones, L. H.; Swanson, B. I.; Eckert, J.; Capps, K. B.; Hoff, C. D. Why Does D_2 Bind Better Than H_2? A Theoretical and Experimental Study of the Equilibrium Isotope Effect on H_2 Binding in a $M(H_2\text{-}H_2)$ Complex. Normal Coordinate Analysis of $W(CO)_3(PCy_3)_2(H_2\text{-}H_2)$. *J. Am. Chem. Soc.* **1997**, *119* (39), 9179−9190.

(20) It is interesting to note that the feasibility of C−N oxidative addition to an in situ generated monovalent nickel species has been demonstrated in a very recent report: Cao, Z.-C.; Xie, S.-J.; Fang, H.; Shi, Z.-J. Ni-Catalyzed Cross-Coupling of Dimethyl Aryl Amines with Arylboronic Esters under Reductive Conditions. *J. Am. Chem. Soc.* **2018**, *140* (42), 13575−13579.

(21) Vabre, B.; Lambert, M. L.; Petit, A.; Ess, D. H.; Zargarian, D. Nickelation of PCP- and POCOP-Type Pincer Ligands: Kinetics and Mechanism. *Organometallics* **2012**, *31* (17), 6041−6053.

(22) Yamamoto, Y.; Chen, X.; Kojima, S.; Ohdoi, K.; Kitano, M.; Doi, Y.; Akiba, K. Experimental Investigation on Edge Inversion at Trivalent Bismuth and Antimony: Great Acceleration by Intra- and Intermolecular Nucleophilic Coordination. *J. Am. Chem. Soc.* **1995**, *117* (14), 3922−3932.

DOI: 10.1021/acs.inorgchem.8b03489
Inorg. Chem. 2019, 58, 3861−3874